Received 00th January 20xx, Accepted 00th January 20xx

DOI: 10.1039/x0xx00000x

www.rsc.org/

Composition-directed Fe_xMo_{2-x}P bimetallic catalysts for hydrodeoxygenation reactions

Dallas J. Rensel, at Jongsik Kim, at Varsha Jain, bt Yolanda Bonita, a Neeraj Rai, bt and Jason C. Hicks at

The development of task-specific bimetallic phosphide catalysts can be accomplished by exploiting the electronic and bifunctional effects of multiple metal combinations, thus providing materials with tunable catalytic properties. Here, we present the modulation of metal compositions (*i.e.*, Fe and Mo) in the synthesis of $Fe_xMo_{2\cdot x}P$ (0.88 \leq X \leq 1.55), leading to a series of *iso*-structural, orthorhombic $Fe_xMo_{2\cdot x}P$ catalysts via reduction at 750 °C. Hydrodeoxygenation of phenol was selected as a probe reaction to showcase the effect of metal composition on the catalytic performance. In particular, catalysts with Fe compositions between 0.99 and 1.14 (*i.e.*, $Fe_{0.99}Mo_{1.01}P$ and $Fe_{1.14}Mo_{0.86}P$) exhibited high selectivities to C-O bond cleavage of phenol with H_2 to form benzene. The catalysts with the highest selectivities to C-O scission also exhibited the highest acidity as determined from NH $_3$ temperature programmed desorption experiments. Density functional theory (DFT) calculations indicate the high Lewis acidity for the ~1:1 Fe:Mo compositions resulted from a greater charge separation between metallic species and P species. These compositions led to greater selectivities to benzene due to desired coordination environment of the phenol on catalytic surface, as evidenced by both DFT calculations and a time on stream study using a benzonitrile poisoner. Enhanced TOFs were also observed with catalysts exhibiting greater Lewis acid character, which reduced the activation energy required to cleave the C-O bond of phenol, as evidenced by DFT calculations. This structure-property study highlights the effects of metal composition in bimetallic phosphides to enhance the activity and selectivity for C-O bond cleavage reactions.

1. Introduction

Bimetallic materials have received significant attention as photovoltaics, ^{1,2} semiconductors, ^{3,4} and catalysts⁵⁻¹¹ because the variation in metal composition can be used as a means to control the electron density, stability, and bi-functionality of the bimetallic materials compared to monometallic materials.⁸ Research has further targeted the synthesis of bimetallic materials through the incorporation of the 3rd atom (*e.g.*,

particular, can be synthesized with a wide variety of metals and compositions of the solid solutions to provide a series of well-defined materials with interesting properties (*e.g.*, FeMoP, ^{21, 22} FeNiP, ²³⁻²⁵ CoNiP, ²⁶ NiMoP, ²⁷⁻²⁹ and RuMoP²⁹). This synthetic versatility can lead to greater control over the surface properties of these materials (*e.g.*, acidity, ^{22, 27, 30, 31} redox, ^{32, 33} and coordination geometry²³⁻²⁵) to serve as solid catalysts. ⁵⁻¹¹

Aside from varying the type of metal species in the bimetallic phosphides, the reduction temperature used for catalyst synthesis can greatly affect catalytic performance.²² We previously synthesized a series of FeMoP catalysts by manipulating the reduction temperatures from 650 °C to 850 °C, which provided different surface acidities. 22 The FeMoP reduced at a lower temperature (650 °C) provided a higher acidity, which in turn exhibited a higher turnover frequency (TOF) for the HDO of phenol compared to other synthesis temperatures.²² In addition, the FeMoP reduced at 650 °C also enhanced the selectivity to benzene (SBENZENE, > 90 %), while minimizing the formation of ring-hydrogenated by-products via tandem reactions (i.e., cyclohexene and cyclohexane).22 Furthermore, time-on-stream experiments provided evidence that FeMoP was stable for at least 48 hours and with pure H₂O pulses due to the surface reduction in the high pressure H2 environment to minimize oxidative deactivation.²² Herein, we have investigated the catalytic properties of FeMoP catalysts as a function of their bulk metal compositions (i.e., Fe and Mo). Previous reports have

- ^a Department of Chemical and Biomolecular Engineering, 182 Fitzpatrick Hall, University of Notre Dame, Indiana 46556, United States.
- ^{b.} Dave C. Swalm School of Chemical Engineering and Center for Advanced Vehicular Systems, Mississippi State University, Mississippi 39762, United States.
- † Authors DJR, JK, and VJ contributed equally.
- * E-mail: jhicks3@nd.edu; Tel: (+1) 574-631-1334.
- * E-mail: neerajrai@che.msstate.edu; Tel: (+1) 662-325-0790.

Electronic Supplementary Information (ESI) available: [reaction mechanisms (HDO2 and HDO3), lattice parameters (Table S1), surface energies (Table S2), molar ratios of Fe to Mo (Table S3), *in situ* DRIFT bands of pyridine (Table S4), bond lengths (Table S5), effect of the change in the K-points grid on activation energy barrier (Table S6), adsorption energies of *n*-alkanes (Table S7), activation energies required for phenol HDO (Table S8), HRTEM images of Fe_{0.99}Mo_{1.01}P (Fig. S1), XP spectra of Fe_XMo_{2.x}P (Fig. S2), *in situ* DRIFT spectra of Fe_{0.99}Mo_{1.01}P (Fig. S3), XP spectra of Fe_{1.55}Mo_{0.45}P post TOS run (Fig. S5),, optimized structures of phenol/benzonitrile/reaction intermediate species and phenol deprotonation on the (112) facets for Fe₁Mo₁P and Fe_{1.5}Mo_{0.5}P (Fig. S4, S6S13)].

borides, 11, 12 carbides, 13, 14 nitrides, 15, 16 oxides, 8, 17 sulfides, 18-20 and phosphides 6, 11, 15) to additionally enhance and control the properties of the resulting materials. Bimetallic phosphides, in

targeted the variation in this synthetic parameter (e.g., $Ni_xMo_{2-x}P$, 28,30 $Co_xNi_{2-x}P$, 26 and $Fe_xNi_{2-x}P^{25}$) and showed the reaction rates and selectivities were substantially affected by composition with optimum values of X ranging from 0.66 to 1.97. 25,26,28,30 These values, however, were greatly dependent on the type of metal species combined to form the bimetallic phosphides, which motivates the need to investigate how composition directs the performance of $Fe_xMo_{2-x}P$ catalysts.

In this study, we synthesized a series of unsupported, isostructural Fe_xMo_{2-x}P hydrodeoxygenation catalysts (Fig. 1 (a)) with X values chosen specifically to minimize any potential effects caused by changes in the bulk structures (Fig. 1 (b)). The effects of composition on the catalytic properties of these Fe_xMo_{2-x}P catalysts were probed using phenol HDO as a model reaction to quantify catalytic performance via turnover frequency (TOF) and selectivity. Additionally, although there are numerous computational studies on HDO on a wide range of metallic and bimetallic catalysts, 34-43 it is not immediately evident in what respects the $Fe_xMo_{2-x}P$ catalysts are similar or different from non-phosphide catalytic systems due to the lack of computational work on bimetallic phosphide catalysts. Therefore, density functional theory (DFT) calculations were performed to gain mechanistic insights into the activity of these Fe_xMo_{2-x}P catalysts, and to understand how phenol interacts with the various catalytic surfaces in these catalysts during the phenol HDO.

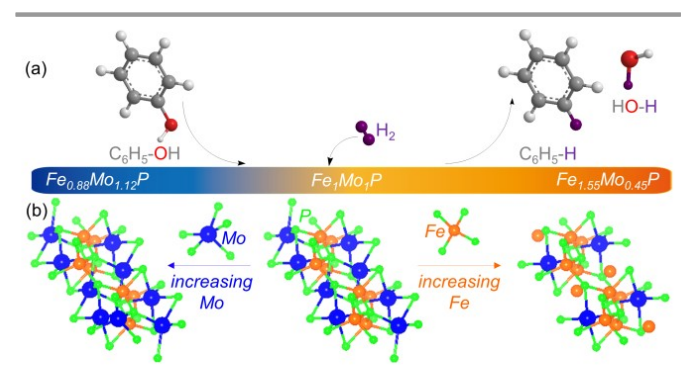


Fig 1 Illustration of (a) hydrodeoxygenation (HDO) of phenol on (b) the catalytic surface of $Fe_xMo_{2\cdot x}P$ with variable bulk metal composition (0.88 $\leq X \leq 1.55$).

2. EXPERIMENETAL AND COMPUTATIONAL SECTION

2.1. Chemicals

All chemicals were used as received from the suppliers: ammonium phosphate dibasic ((NH₄)₂HPO₄, Ameresco, 98%), phenol (Sigma Aldrich, 99%), iron nitrate nonanhydrate (FeNO₃·9H₂O, Alfa Aesar, 99%), ammonium molybdate tetrahydrate ((NH₄)₆MO₇O₂₄•4H₂O, Alfa Aesar, 99%), *n*-decane (Alfa Aesar, 99%), benzonitrile, ICP standards Fe, Mo, and P (Ultra Scientific, 1,000 mg mL⁻¹), and Si standard (Alfa Aesar, ~ 170 mesh). Pyridine (Alfa Aesar, 95+ %) was dried using 4 Å molecular sieves prior to its utilization. Gas cylinders were purchased from Airgas (\geq 99.995%): Ar, He, H₂, 1% O₂ in He, 2% NH₃ in He, and 30% CO in He.

2.2. Synthesis

FeMoP catalysts were synthesized by following a slightly modified procedure from our previous studies.^{21, 22} The FeNO₃·9H₂O, (NH₄)₆Mo₇O₂₄•4H₂O, and (NH₄)₂HPO₄ precursors were added to an aqueous, citric acid solution (0.4 M) in the ratios based on the desired Fe:Mo:P composition. A rotary evaporator was used to partially dry the mixture to a viscous solution, which was then moved to crucible bowl. The material was then heated in an air atmosphere with a ramp rate of 1.5 °C min⁻¹ to 200 °C and held at 200 °C for an hour. The resulting brown solid was ground into a powder and calcined in an air atmosphere by ramping to 550 °C with a ramp rate of 1 °C min⁻¹ and holding at 550 °C for six hours. The resulting powder was reduced under a flow of H₂ with a rate of 160 mL min⁻¹ inside a quartz tube in a tube furnace. The following reduction procedure was employed: ramp to 100 °C at 5 °C min-1 held at 100 °C for an hour, ramp to 260 °C at 5 °C min⁻¹ held at 260 °C for an hour, and ramp to 750 °C at 5 °C min⁻¹ held at 750 °C for two hours. After reduction, the resulting catalyst was cooled to room temperature under a H2 atmosphere, passivated using a 1% O₂/He with the flow rate of 60 mL min⁻¹ for an hour, and stored inside a nitrogen dry box.

2.3. Characterization

X-ray diffraction (XRD) patterns were collected with a Bruker DaVinci Advanced D8 X-ray diffractometer using a Cu Kα radiation source (λ = 1.5418 Å). The scan parameters were 20 range of 20-60°, scan speed of 2.5 second per step, and a size step of 0.01° per step. Bulk catalyst composition was quantified using a Perkin Elmer Optima 2000 DV inductively coupled plasma-optical emission spectrometry (ICP-OES) with external calibration curves of Fe, Mo, and P. High resolution transmission electron microscopy (HRTEM) images, selected area electron diffraction pattern (SAED), and energy-dispersive X-ray (EDX) spectra of Fe_{0.99}Mo_{1.01}P were acquired on a FEI Titan 80-300 microscope at 300 keV, while following a procedure described in our previous works. 21, 22 Diffuse reflectance Infrared Fourier transform spectroscopy (DRIFTS) analysis was performed with a Harrick Praying Mantis™ cell and a Jasco FT/IR-6300 spectrometer, while following a procedure slightly modified based on our previous work.44 The Fe_{0.99}Mo_{1.01}P was dispersed in *n*-hexanes, mixed with silica with a loading of 15 wt. %, loaded into a cell, and sealed inside a N₂ glove box. The cell including Fe_{0.99}Mo_{1.01}P was removed from the glove box and initially heated to 150 °C under a N₂ atmosphere with a ramp rate of 10 °C min-1. After collecting the background spectrum of Fe_{0.99}Mo_{1.01}P, a pyridine saturated N₂ stream was passed over the Fe_{0.99}Mo_{1.01}P sample at 150 °C for 45 minutes. The gas stream was then switched to only $N_{\scriptscriptstyle 2}$ in order to remove gaseous or physisorbed pyridine on the Fe_{0.99}Mo_{1.01}P surfaces. NH₃ temperature programmed desorption (NH₃-TPD) experiments performed based on a modified procedure depicted in our previous works, 45, 46 while using a Micromeritics Chemisorb 2750 operated with a thermal conductivity detector (TCD) and TPx temperature controller. The catalyst was re-reduced under a flow of H₂ (110 mL min⁻¹) by ramping at 10 °C min⁻¹ to 400 °C for two hours followed by 1.5 hours under a flow of He (80 mL min⁻¹) at 400 °C. Chemisorption of NH₃ was performed by

flowing a 2 % NH₃ in He (80 mL min⁻¹) over the catalyst at 100 °C for 2 hours. Subsequently, NH₃ desorption was performed under a He atmosphere by ramping at 10 °C min. 1 to 230 °C, holding at 230 °C for 42 minutes, ramping at 10 °C min. 1 to 400 °C, and holding 400 °C for 42 minutes. The desorbed area was quantified based on NH₃ calibrations using a 2% NH₃ in He. CO pulsed chemisorption experiments were conducted on the Micromeritics Chemisorb 2750 instrument following the same pre-treatment steps as that used to perform NH₃-TPD experiments. Pulse of CO was introduced to the catalyst at 35 °C using 0.1 mL injections of a 30% CO in He. The amount of CO uptake on each catalyst was obtained based on the area of each peak and subsequently quantified based on CO calibrations using a 30% CO in He.47 Brunauer-Emmett-Teller surface area (S_{BET}) of the catalysts was analyzed using a Quantachrome Nova 2200e. A PHI VersaProbe II X-ray Photoelectron Spectrometer was employed to obtain X-ray photoelectron (XP) spectra of the catalysts to analyze the surface species with a C 1s as a reference peak located at 284.5 eV.

2.4. Reaction conditions

Hydrodeoxygenation reactions were performed in a continuous flow reactor in an up flow configuration.²² In a typical experiment, 30 mg of the catalyst particles were diluted using 100 mg of Davisil® grade 635 silica gel and subsequently packed in a 316 stainless steel reactor, while using a stainless mesh steel screen (10 μm, McMaster-Carr) and quartz wool (VWR Scientific) to immobilize the catalyst particles in the reaction control volume. For the rate comparison, the reactor was operated in the forward reaction-dominant regime at ≤ 15% conversion of phenol.²² The flow rates of the reactant solution (0.13 M of phenol dissolved in n-decane) was controlled using a high pressure liquid chromatography (HPLC) pump (Hitachi L-6000), the flow rate of H₂ (100 mL min⁻¹) was regulated via a mass flow controller (Aalborg GFC17). Reaction temperature was adjusted using PID controllers and maintained at 400 °C using a heat tape (Omega Engineering). Phenol HDO reactions were operated in excess H2 with the molar feed ratio of H2 to phenol of ~34. A time on stream (TOS) experiment using Fe_{1.55}Mo_{0.45} was performed identically to the phenol HDO detailed above except reactant mixtures of benzonitrile and phenol were fed into the reactor at pre-determined reaction times. Three different reactant mixtures were prepared with molar ratios of benzonitrile to phenol as 1:2, 1:1, and 10:1, while maintaining a constant molar concentration of phenol. Products were quantified using an Agilent 7890A gas chromatograph (GC) directly coupled to an Agilent 5975C mass spectrometer (MS) and based on external calibration curves. Throughout all reaction runs, the carbon balance was ≥ 95%. Selectivity and TOF were calculated based on Eqn. (1) and (2), respectively.

$$selectivity = \frac{moles\ of\ specific\ product}{moles\ of\ all\ products} \times 100(1)$$

$$TOF = \frac{moles \ of \ reactant \ consumed}{moles \ of \ CO \lor NH_3 - accessible \ sites \times minutes}$$

2.5. Computational methodology

The plane wave periodic density functional theory (DFT)^{48, 49} calculations within the supercell were performed using Vienna ab initio simulation package (VASP). 50-53 The exchangecorrelation energy was calculated within the generalized gradient approximation (GGA) using Perdew-Wang 91(PW91) functional.54-56 The core electrons are described with the projector augmented waves (PAW) method^{57, 58} to solve the Kohn-Sham equations. 58, 59 The energy cut-off was taken as 450 eV to ensure high precision. Total energies were calculated using a first-order Methfessel–Paxton smearing function⁶⁰ with a width of 0.1 eV. Optimizations were carried out until the net forces acting on atoms were smaller than 0.03 eV Å-1. Spinpolarization was included in all calculations with Γ-point sampling of Brillouin zone. 61 To see the effect of K-point sampling, calculations were performed with a grid of 2 X 2 X 1. The activation energy barriers for C-O bond cleavage obtained for Γ-point and 2 X 2 X 1 grids were virtually identical with differences ≤ ~ 0.001 eV (Table S6). Crystal structures of two Fe_xMo_{2-x}P catalysts (i.e., Fe₁Mo₁P with X=1; Fe_{1.5}Mo_{0.5}P with X=1.5) were optimized with 2 X 4 X 2 supercell (Fig. 2 (b)) based on cell parameters determined via XRD patterns of these catalysts (Fig. 3). Optimized unit cell parameters in these catalysts showed a deviation of ≤ 1 % in comparison with those experimentally determined (Table S1) except for the cell parameter of b for $Fe_{1.5}Mo_{0.5}P$ exhibited a deviation of $\sim 2\%$. Throughout the optimization, the crystal plane of (112) was considered because (112) was observed as the most dominant facet in the XRD patterns of these materials (Fig. 3). The (112) facet had the lowest surface energy for both compositions based on DFT calculations (Table S2). The surface on the (112) plane was modeled with a slab containing six atomic layers and with a supercell size P (2 X 2) (Fig. 2 (c)). Throughout the calculations, the bottom two layers of the slabs were fixed to represent the corresponding crystal structure, whereas all other atoms in the systems were relaxed in all degrees of freedom. A vacuum height of 15 Å was employed over the slabs and the reactive species were optimized on only one side of the slab. The number of phosphorus atoms was maintained constant (48 atoms) for all the calculations, whereas the number of Fe and Mo atoms was governed by the stoichiometry. The adsorption energies (denoted as E_{ADS}) were calculated according to Eqn. (3), wherein E_{ADSORBATES+SURFACE} is defined as the total energy of species adsorbed on the surface; ESURFACE is defined the total energy of surface; and EADSORBATES is defined as the energy of the adsorbed species on the surface in the gas phase.

$$E_{ADS} = E_{ADSORBATES + SURFACE} - E_{SURFACE} - E_{ADSORBATES}(3)$$

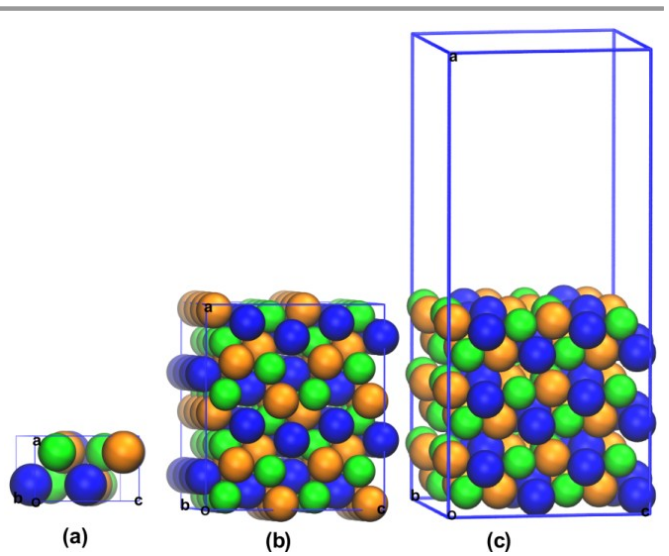


Fig. 2 Optimized orthorhombic crystal structure of Fe_1Mo_1P : (a) unit cell, (b) 2 X 4 X 2 supercell, and (c) surface on (112) plane (orange for Fe; blue for Mo; green for P).

Phenol, benzonitrile, and a series of alkanes (ethane to heptane) were considered as adsorbates to understand their relative coverage on the surface. Transition states for elementary steps in the minimum energy pathways (MEP) were identified using the nudged elastic band (NEB) method, $^{62-64}$ and these were further refined with the climbing image nudged elastic band (CINEB) method. 65 Transition states were confirmed by examining vibrational frequencies (presence of only one imaginary frequency). The activation energy barrier (denoted as $E_{\rm ACTIVATION}$) with respect to each transition energy state ($E_{\rm TRANSITION}$) were calculated by Eqn. (4), where $E_{\rm REACTANT}$ denotes the total energy of reactant.

$$\boldsymbol{E}_{\textit{ACTIVATION}}\!=\!\boldsymbol{E}_{\textit{TRANSITION}}\!-\!\boldsymbol{E}_{\textit{REACTANT}}(\mathbf{4})$$

Since our goal was to compare the mechanistic pathways (rather than the absolute rates) on the surface of the catalysts with two different compositions, we have only considered electronic energies, and the thermal and coverage effects were not included.

3. Results and discussion

3.1. Bulk properties of Fe_xMo_{2-x}P catalysts

For the synthesis of Fe_xMo_{2-x}P catalysts with different X values ranging between 0.88 and 1.50, the required amounts of Fe and Mo precursors were dissolved in an aqueous citric acid solution. It was previously reported that *iso*-structural Fe_xMo_{2-x}P materials can be synthesized with 0.60 < X < 1.64. ⁶⁶ Therefore, we selected the 0.88 - 1.50 range of X to ensure a single solid solution for each composition. The resulting dried mixtures were subsequently calcined prior to their reduction with H₂. Attempts to synthesize the final Fe_xMo_{2-x}P materials via reduction of the intermediates at 650 °C evolved additional bulk

phases assigned to iron-molybdenum oxides except for Fe₁Mo₁P. In addition, the Fe₁Mo₁P material reduced at 850 °C provided a lower concentration of CO-titrated surface sites than other Fe₁Mo₁P analogues reduced at lower temperatures.²² Therefore, our experimental focus was to synthesize the Fe_xMo_{2-x}P materials via reduction of the intermediates at 750 °C for consistency amongst all material compositions. Inductively coupled plasma-optical emission spectroscopy (ICP-OES) was used to determine the bulk composition of Fe, Mo, and P present in the catalysts, which provided values of 0.88, 0.99, 1.14, 1.26, and 1.55 for X, which were in good agreement with the theoretical values of 0.88, 1.00, 1.13, 1.25, and 1.50, respectively. Fe_{0.99}Mo_{1.01}P shows a crystalline feature of the typical FeMoP from high resolution transmission electron microscopy (HRTEM) analysis, which is in line with our previous reports (Fig. S1).^{21,22} The images exhibit a series of parallel lattice fringes resulting from the [111] zone axis of FeMoP, which is identified via selected area electron diffraction (SAED) analysis. Of note, the bulk ratio of Fe to Mo found in Fe_{0.99}Mo_{1.01}P (0.98 (± 0.08)) is retained even in its surfaces, which is evidenced by two complimentary surface characterizations such as energydispersive X-ray (EDX) spectroscopy (1.06 (± 0.15)) and X-ray photoelectron (XP) spectroscopy (1.06 (± 0.05) in Table S3). In addition, Powder X-ray diffraction (XRD) provided evidence that the various compositions studied here yielded iso-structural forms of FeMoP (Fig. 3). As shown in Fig. 3, all the catalysts showed diffractions assigned to the crystal planes of orthorhombic FeMoP (PDF No.: 04-001-4367), with the (112) facet as the most dominant plane (shown with red circle). This is in good agreement with the lowest surface energies on the (112) plane for both Fe₁Mo₁P and Fe-rich Fe_{1.5}Mo_{0.5}P materials computed via DFT calculations, as specified in Table S2.

Lattice parameters of Fe $_{0.99}$ Mo $_{1.01}$ P (a = 5.92 Å; b= 3.65 Å; c=6.78 Å) were well-matched to those of FeMoP calculated using the PDF (a = 5.92 Å; b= 3.66 Å; c=6.79 Å in 1 X 1 X 1 unit cell). In addition, the shift in peak locations to lower values of 20 was observed for decreasing amounts of Fe in the structure (X of $1.55 \rightarrow 0.88$ in Fig. 3). This shift was caused by the substitution of Fe atoms with larger Mo atoms in the FeMoP lattice, which in turn increases the lattice parameters of the resulting unit cells. As quantified by Whole Pattern Fitting (WPF) using Jade software (Fig. 4), $^{67, 68}$ it was evident that the decrease in the Fe composition led to an increase in lattice parameters (*i.e.*, a of 5.88 Å \rightarrow 5.93 Å; b of 3.61 Å \rightarrow 3.66 Å; c of 6.70 Å \rightarrow 6.80 Å).

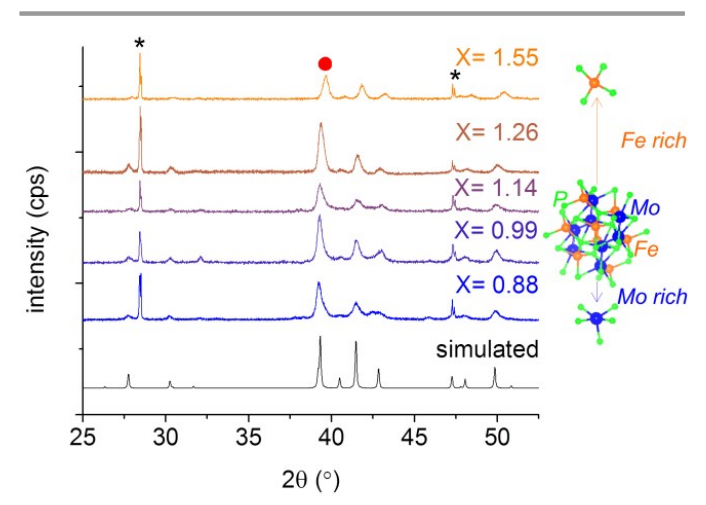


Fig. 3 XRD patterns of $Fe_xMo_{2:x}P$ and simulated Fe_1Mo_1P (PDF No.: 04-001-4367). The red circle indicates (112) diffractions observed in these catalysts. Peaks labeled with * indicate diffractions of the Si standard.

These shifts are in agreement with a previous study on orthorhombic $Fe_xMo_{2.x}P$ catalysts (X of $0.62 \rightarrow 1.64$), which also showed the inclusion of the larger Mo atom via exchange with Fe decreased the values of $20^{.66}$ Notably, a linear trend in a with respect to the X value was obtained (Fig. 4), which indicated $Fe_xMo_{2.x}P$ catalysts followed Vegard's Law within the X range provided in this study. Finite linear relationship was consistent with other types of bimetallic phosphides previously reported (e.g., NiMoP²⁰ and FeMoP⁶⁶) and suggested the $Fe_xMo_{2.x}P$ catalysts comprised a solid solution.

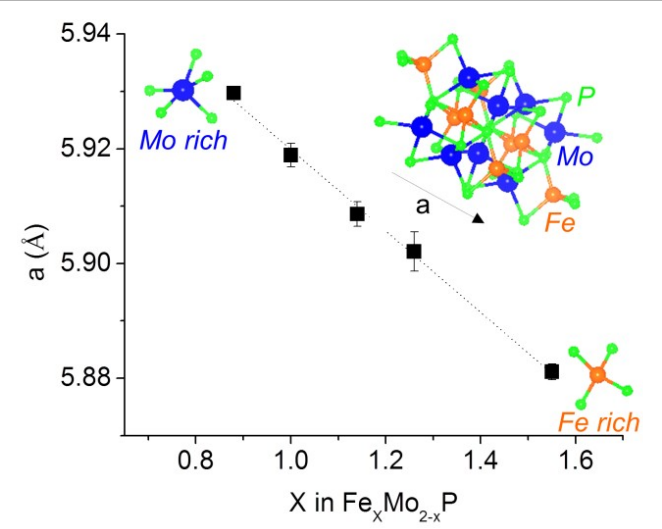


Fig. 4 Unit cell parameter, a (Å), obtained through the variation in the amount of Fe (X) in Fe_XMo_{2-X}P.

3.2. Surface properties of Fe_xMo_{2-x}P catalysts

The properties of the $Fe_xMo_{2-x}P$ powders on/near the surface was analyzed via X-ray photoelectron (XP) spectroscopy that has been widely employed for exploring the elemental composition near the surface of metal phosphides. ^{11, 33, 71} As shown in Fig. 5 and S2, Fe, Mo, and P species near the surface were quantified based on their relative abundances in the Fe $_{2p}$, Mo $_{3d}$, and P $_{2p}$

regions, respectively. Each material exhibited a similar abundance of surface P species across all catalysts (38-40 mol. %). However, as expected, the increase in the bulk Fe content (i.e., X of $0.80 \rightarrow 1.55$) resulted in an increase in surface Fe species (27 % → 47 %, orange rectangles in Fig. 5). This links to the trend shown in Table S3, which shows bulk molar ratios of Fe to Mo across all Fe_xMo_{2-x}P materials are in close agreement with those obtained from XPS. In transition metal phosphides, the electronegative P atoms attract the electrons of the metals (denoted as M) to distribute surface charges of the phosphide materials to produce surface $M^{\delta +}$ species and $P^{\delta -}$ species (δ indicates a partial charge), $^{32, \, 33, \, 71}$ where surface $M^{\delta +}$ species can behave as Lewis acid sites. 18, 35, 72, 73 Of note, the inclusion of two different surface metal species in bimetallic phosphide materials can provide additional charge transfer among these metals due to the difference in their electronegativities, which was hypothesized based on computational studies of bimetallic alloys (Allred-Rochow electronegativity values of 1.64 for Fe and 1.30 for Mo).74, 75 Additionally, other reported studies on phosphide materials demonstrated the charge transfer between metals can be significantly directed by their relative composition.^{32, 76} Therefore, it was hypothesized that a change in the composition of surface metal species on Fe_xMo_{2-x}P catalysts could alter the amount of Lewis acid sites via multiple, different contributions of charge transfer among surface metal species. However, using XPS analysis to determine shifts in electron densities between two surface metal species in transition metal phosphides based on their binding energies is inconclusive due to the screening effect induced by the shared valence electrons in these materials.33,76 Thus, despite observing the shift in binding energies for all surface species in the XP spectra of the Fe_xMo_{2-x}P catalysts (Fig. S2), the binding energy values only differ by < 0.2 eV and therefore cannot be used as a quantitative technique to compare the values.

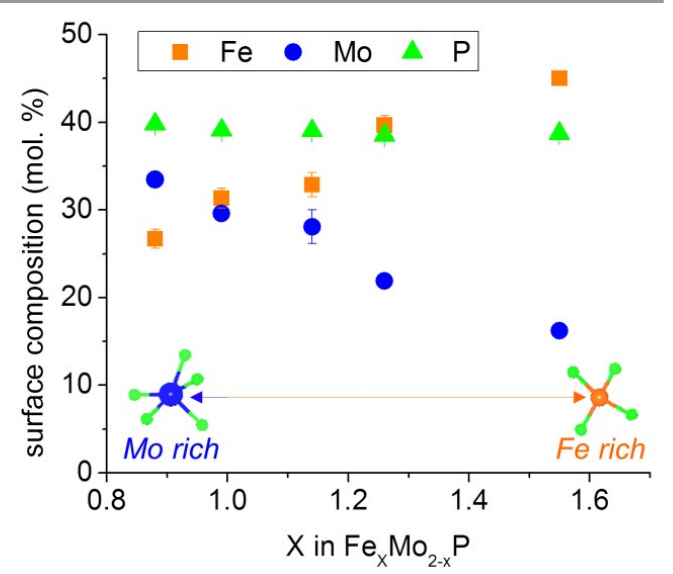


Fig. 5 XPS analysis of surface Fe, Mo, and P species present in Fe_XMo_{2-X}P.

We, therefore, performed Bader charge analysis⁷⁷⁻⁸⁰ to gain further insights into the charge distribution between metal

species and P species on the (112) facet for Fe₁Mo₁P and Fe_{1.5}Mo_{0.5}P, both of which were chosen based on values of X observed in Fe_xMo_{2-x}P materials via ICP-OES experiments (i.e., 0.99 and 1.55, respectively). The crystal plane of (112) was also selected because (112) was the most dominant plane observed in Fe_xMo_{2-x}P catalysts, as evidenced by their XRD patterns (Fig. 3). Bader charge analysis provided evidence that electron transfer from metallic to phosphorus species was directed by the composition of metals, as evidenced by the values of partial atomic charges on both catalysts (i.e., +0.81 |e| for Fe, Mo, and -0.81 |e| for P in Fe₁Mo₁P; +0.63 |e| for Fe, Mo, and -0.63 |e| for P in Fe_{1.5}Mo_{0.5}P, where |e| denotes the charge on an electron). The charge separation was more pronounced on the Fe₁Mo₁P surface than the Fe-rich Fe_{1.5}Mo_{0.5}P surface, which indicated that Fe₁Mo₁P could possess a greater Lewis acid feature than $Fe_{1.5}Mo_{0.5}P$. In addition, partial charges on Mo were consistently larger than those of Fe in both catalysts (i.e., +0.07 |e| for Fe and +0.74 |e| for Mo in Fe₁Mo₁P; +0.11 |e| for Fe and +0.52 |e| for Mo in Fe_{1.5}Mo_{0.5}P). Thus, while ignoring steric effects, Mo appeared to be a stronger Lewis acid site than Fe, which again was in line with the smaller Allred-Rochow electronegativity of Mo than Fe.^{74, 75}

In situ diffuse reflectance infrared Fourier transform (DRIFT) spectroscopy was employed to qualitatively investigate the acidity of Fe_{0.99}Mo_{1.01}P. Pyridine served as a probe molecule to bind with acid sites via coordination or protonation, thus yielding distinct absorption bands in the resulting in situ DRIFT spectrum (Fig. S3 and Table S4). 31,81,82 The presence of Lewis acid sites on Fe_{0.99}Mo_{1.01}P was evidenced by a discernable absorption band located at ~ 1445 cm⁻¹, which resulted from pyridine/Lewis acid site interactions. 31, 81, 82 Weak features located at 1490 and 1550 cm⁻¹ were observed for the interaction of pyridine with surface Brønsted acid sites, both of which resulted from protonated pyridine species (pyridinium).31, 81, 82 To further investigate the acidity of Fe_xMo_{2-x}P catalysts, NH₃ temperatureprogrammed desorption (NH3 TPD) was alternatively used to titrate the accessible Brønsted acid and Lewis acid sites and thus provide the total amount of surface acid sites on these catalysts.^{28,72} Notably, surface P species have been suggested as a primary source of surface Brønsted acid sites on transition metal phosphides. 30, 31 Table 1 details the total amount of surface acid sites accessible to NH₃ in the catalysts (denoted as N_{ACID}) with the normalization on the Brunauer-Emmett-Teller surface area (SBET). Aside from showing greater Lewis acid character from the Bader charge analysis, both $Fe_{0.99}Mo_{1.01}P$ and $Fe_{1.14}Mo_{0.86}P$ catalysts also showed larger values of N_{ACID} (≥ 3.8 µmol m⁻²) compared to the others (≤ 3.6 µmol m⁻²).

Table 1 Surface properties of Fe_xMo_{2-x}P.

X in	S _{per} ^a	number of surface sites

Fe _x Mo _{2-x} P	(m ² g ⁻¹)	N _{ACID} ^{b,d} (μmol m ⁻²)	N _{co} ^{c,d} (μmol m ⁻²)
1.55	2.1 (± 0.2)	3.0 (± 0.2)	4.6 (± 0.2)
1.26	3.3 (± 0.3)	3.2 (± 0.2)	2.9 (± 0.2)
1.14	3.7 (± 0.2)	4.5 (± 0.3)	4.3 (± 0.1)
0.99	4.0 (± 0.4)	3.8 (± 0.2)	3.5 (± 0.1)
0.88	5.8 (± 0.6)	3.6 (± 0.2)	3.1 (± 0.1)

 $^{^{\}alpha}$ BET surface area. b NH₃-accessible sites from NH₃ TPD. c CO-accessible sites from CO-pulsed chemisorption. $^{\sigma}$ normalized with respect to S_{BET}.

CO-pulsed chemisorption experiments were also performed on these materials to quantify total amount of surface metal sites accessible to CO. 83,84 Interestingly, as shown in Table 1, the largest amount of CO-accessible surface sites normalized on S_{BET} (denoted as N_{CO}) was observed in the Fe_{1.55}Mo_{0.45}P catalyst (*i.e.*, X = 1.55). This was in contrast to the trend found from the Bader charge calculation or NH₃ TPD experiment which showed Lewis acid strength and the titrated amount of surface acid sites were greater, when X was near unity in Fe_xMo_{2.x}P catalysts.

To determine the catalytic consequences of the metal composition, hydrodeoxygenation (HDO) of phenol was used to compare all synthesized Fe_xMo_{2-x}P materials. The choice of this reactant was based on previous studies which showed HDO of phenol was strongly associated with the surface metal sites (quantified as N_{CO})^{18, 22, 72} or (Lewis acid) metal sites combined with Brønsted acid sites (quantified as N_{ACID}).^{39, 85-87} The reaction was performed using a flow reactor at 400 °C with H₂ pressure of 52 bar in the reaction-limited regime. To investigate the effect of the amounts of surface metal sites on Fe_xMo_{2-x}P catalysts during the reaction, phenol consumption rates were normalized on N_{co} (turnover frequency denoted as TOF_{co}) and compared. Similar to our previous work, 22 it was observed here that surface metal sites on the catalysts are responsible for catalyzing the phenol HDO to form benzene, when X was varied from 0.88 to 1.26. As shown in Fig. 6 (a), higher TOF_{co} values are observed in $Fe_XMo_{2-X}P$ catalysts that possessed ~ 1:1 Fe:Mo ratios. Both $Fe_{0.99}Mo_{1.01}P$ and $Fe_{1.14}MoP_{0.86}P$ exhibited large N_{CO} values of ~ 3.9 μmol m⁻² and therefore exhibited higher TOF_{co} (~ 12 min⁻¹) than the other compositions. Despite having the greatest N_{co} among all catalysts ($^{\sim}$ 4.6 μ mol m $^{-2}$), Fe_{1.55}Mo_{0.45}P showed the lowest TOF_{co} as ~ 5.3 min⁻¹. This result suggested the amount of surface metal sites (i.e., N_{CO}) in Fe_xMo_{2-x}P catalysts may not be a sole source to direct the phenol consumption rate. Another viable source to control phenol HDO is the strength of the Lewis acid sites in these catalysts because stronger Lewis acidity can enhance the interaction between the O atom of phenol with the surface, weaken its CAROMATIC-O bond and therefore facilitate C_{AROMATIC}-O scission, as reported previously.^{8,85} Hence, it can be conjectured that the weaker Lewis acid feature found on Fe-rich Fe_{1.55}Mo_{0.45}P materials in comparison with analogues with lower Fe composition (e.g., Fe_{0.99}Mo_{1.01}P) can reduce the TOF_{CO}. This, again, is in line with Bader charge analysis of Fe_xMo_{2-x}P catalysts, which verifies stronger Lewis acid character on Fe₁Mo₁P than $Fe_{1.5}Mo_{0.5}P$.

Transition metal phosphides are multi-functional materials with multiple possible surface functionalities present that could facilitate phenol HDO including Brønsted acid sites (i.e., P-OH)

and Lewis acid sites. Both of these surface moieties can participate in the reaction by weakening the $C_{AROMATIC}$ -O of phenol via either protonation (Brønsted acid site) or adsorption of the O in phenol (Lewis acid metal site). Therefore, although the major source for catalyzing phenol HDO is likely the surface Lewis acid sites present in the Fe_xMo_{2-x}P catalysts, the phenol consumption rates were also normalized with respect to N_{ACID} (denoted as TOF_{NH3}) and shown in Fig. 6 (b). It is evident from Fig. 6 that normalization on CO titrated sites or NH_3 titrated sites provides a nearly identical trend in rates as a function of metal composition and nearly similar magnitudes. Additionally, the $Fe_xMo_{2-x}P$ catalysts with larger N_{ACID} provided greater TOF_{NH3} values.

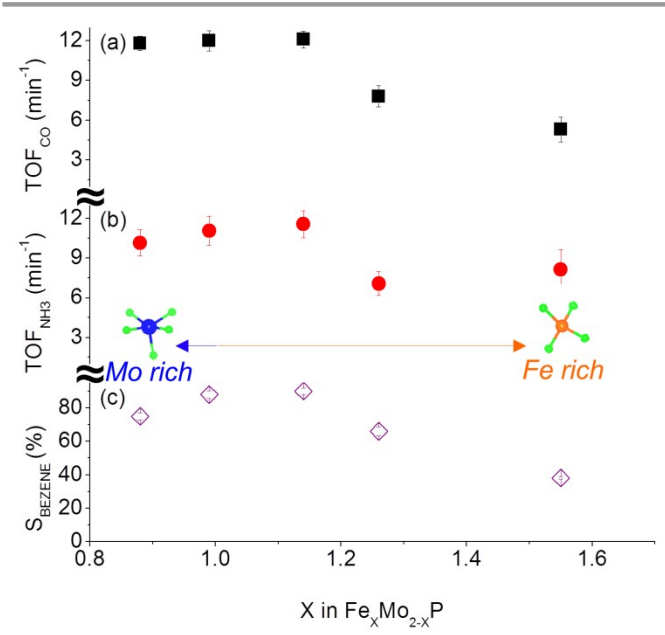


Fig. 6 Turnover frequencies normalized with number of active sites identified with different probe molecules as well as benzene selectivity as a function of composition. (a) TOF_{CO} , (b) TOF_{NH3} , and (c) $S_{BENZENE.}$ on $Fe_xMo_{2:x}P$ during phenol HDO.

Notably, aside from exhibiting the highest TOF_{CO} and TOF_{NH3} values, both $Fe_{0.99}Mo_{1.01}P$ and $Fe_{1.14}Mo_{0.86}P$ also provided the highest selectivities to benzene (Fig. 6 (c)). From these experiments and trends in TOFs normalized on either NH_3 or CO, the Lewis acidic metal surface is a primary contributor to the catalytic performance of these materials. To further investigate the effects of the Lewis acidic metal surfaces on the TOF and the $S_{BENZENE}$ during phenol HDO, reactions were performed using various poisons (pyridine or CO) to compete with active sites on the catalytic surface. These experiments, however, were unsuccessful due to the high activities of these catalysts to perform either hydrodenitrogenation of pyridine 88 or hydrogenation of CO^{89} under the reaction condition employed.

Thus, we employed benzonitrile (C_6H_5CN) as an alternative, in situ surface poison. The selection of benzonitrile was based on its structural similarities to phenol (kinetic diameter of ~6.1 and 6.2 Å for phenol and benzonitrile, respectively)^{90, 91} and the ability to compete for the adsorption on Lewis acid sites from

the nitrile group. DFT calculations on the (112) facet for Fe₁Mo₁P and Fe_{1.5}Mo_{0.5}P provided evidence that benzonitrile and phenol bind with the catalytic surfaces in a similar manner. As shown in Fig. S4, these two molecules exhibit comparable adsorption energies on the (112) facet under identical binding configurations. It should be noted that interactions between *n*decane (reaction solvent) and the catalytic surface are negligible, as evidenced by insignificant adsorption energy of the smaller *n*-alkanes homologues (ranging between -0.17 eV and -0.24 eV in Table S7) in comparison with the phenol and the benzonitrile (-1.3 eV to -1.6 eV). The DFT calculations, therefore, motivated a time on stream (TOS) experiment, where benzonitrile was co-fed with phenol during HDO on $Fe_{1.55}Mo_{0.45}P$, while monitoring $S_{BENZENE}$ under transient and steady state operation. Therefore, molar ratios of benzonitrile to phenol were varied during this experiment (denoted as 1:2, 1:1, and 10:1) using the Fe-rich catalyst (Fig. 7). Conversions of phenol decreased from ~4 % to ~0.5 % during the TOS experiment due to the continuous exposure of the catalytic surfaces to benzonitrile. This resulted in the production of surface Fe-N and Mo-N species that were less active to the phenol HDO in comparison with the surface metal phosphide counterparts. This is evidenced by the XP spectrum of Fe_{1.55}Mo_{0.45}P after the TOS experiment, which showed the retention of reduced states for surface Fe and Mo species, the elimination of surface reduced P species, and the production of surface reduced N species binding with metals (Fig. S5). 92-94 However, from the TOS experiment, competitive adsorption of phenol and benzonitrile onto the catalytic surfaces directly altered S_{Benzene} (Fig. 7). This is evidenced by the increase in S_{BENZENE} from ~40 % to ~80 % upon the change in the feed solution from only phenol to the 1:2 benzonitrile:phenol mixture. It should be noted that a sole source of benzene during this experiment is phenol, as indicated by carbon balance among the phenol, benzene, and hydrogenated by-products to be close at ≥ ~ 95 %. In addition, the increase in S_{BENZENE} is more pronounced at greater molar ratios of benzonitrile to phenol (i.e., $S_{BENZENE}$ of \sim 95 % at 1:1 and \sim 100 % at 10:1). This interesting result was likely due to the change in the binding configuration of phenol in the presence of benzonitrile. In addition to the DFT calculations, the TOS experiment suggests that the surface interactions can be modulated with reactant additives to provide preferential binding of phenol to increase SBENZENE in Ferich Fe_xMo_{2-x}P, which remains a topic of study in our laboratory.

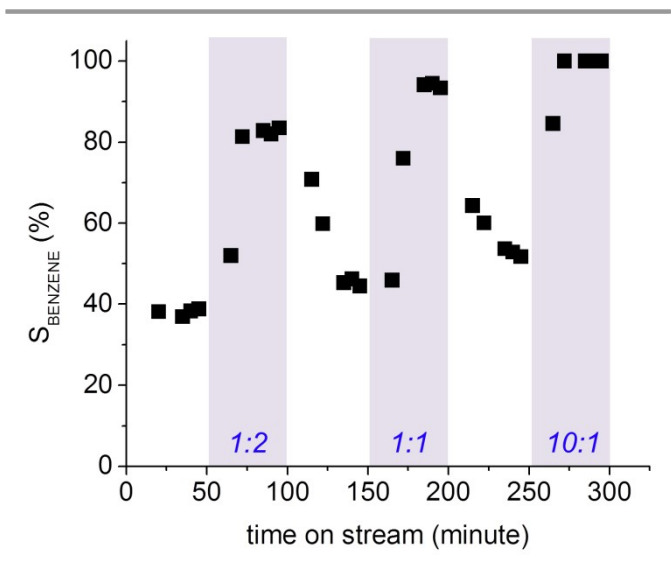


Fig. 7 Benzene selectivities (S_{BENZENE}) on Fe_{1.55}Mo_{0.45}P during a time on stream (TOS) study using either phenol only or benzonitrile/phenol mixtures with variable molar ratios ranging from 1:2, 1:1 to 10:1. Purple-shaded regions indicate when the reactant mixtures were fed into the reactor.

3.3 Mechanistic investigation of phenol HDO on $Fe_xMo_{2\cdot x}P$ catalysts

Following the combined experimental/ computational studies to investigate different S_{BENZENE} in Fe_xMo_{2-x}P catalysts, three different plausible reaction mechanisms of the phenol HDO on (112) facets for both Fe₁Mo₁P and Fe_{1.5}Mo_{0.5}P catalysts were investigated. The purpose of these DFT calculations is to better understand the mechanistic role of surface Lewis acidity in these catalysts in directing TOFs for $C_{\mbox{\scriptsize AROMATIC}}\mbox{\scriptsize -}O$ bond cleavage. These mechanisms were chosen based on previous experimental²² and computational studies,^{38, 39, 42} all of which detailed the mechanistic aspects of catalytic HDO of lignin model compounds on monometallic (e.g., Fe^{38, 95}, Pd,³⁸ Pt,^{11, 88} Ru,^{39, 40, 89} and Rh^{42, 88}) and bimetallic alloy surfaces (e.g., Ni-Fe,^{37,} ⁴³ Co-Mo,³⁵ and Pd-Fe⁹⁵). HDO1 was identified as the most feasible mechanism because this mechanism provides the lowest activation energies for both Fe_1Mo_1P and $Fe_{1.5}Mo_{0.5}P$ in the rate-determining steps among all different mechanisms investigated in this study (Table S8). Thus, the HDO1 is mainly discussed in this section (HDO1), whereas the other two HDO mechanisms are specified in the Supplementary Information (HDO2 and HDO3, see Fig. S7-S10).

The specific HDO1 reaction pathways are illustrated in Eqn. (5)-(10) on the catalytic surface of Fe₁Mo₁P (Fig. 8) and Fe_{1.5}Mo_{0.5}P (Fig. S6). The HDO1 involves the production of intermediate phenyl species (C₆H₅), which is reduced to generate benzene (C₆H₆) via addition of surface H species, while producing H₂O species as a by-product.^{38, 39, 41} Initially, phenol (C₆H₅OH) is only adsorbed on surface Lewis acid sites (*i.e.*, Fe-Mo interface) to form C₆H₅OH* (Eqn. (5) and Table S5). In addition to *n*-decane (reaction solvent) incapable of deprotonating phenol due to its high pKa dissolved in *n*-decane (*i.e.*, > 18), it is also unlikely to deprotonate C₆H₅OH* to evolve phenoxide (C₆H₅O*)

and H*. This is evidenced by DFT calculations associated with $C_6H_5OH^*+^* \leftrightarrow C_6H_5O^* + H^*$ on (112) facets for $Fe_xMo_{2-x}P$ materials (Fig. S12 and S13). For this reaction, the forward direction requires far greater activation energies (~ 0.54 eV) than the reverse direction (~0.06 eV). Instead, as shown in Fig. 8 (a) and S6 (a), the O atom of C₆H₅OH is adsorbed on surface sites with the average distances between phenol and the surfaces as 2.3 Å and 2.1 Å for Fe₁Mo₁P and Fe_{1.5}Mo_{0.5}P, respectively. This adsorption step also provides adsorption energies of C₆H₅OH as -1.37 eV and -1.63 eV for Fe₁Mo₁P and Fe_{1.5}Mo_{0.5}P, respectively, all of which are in a similar range as previous works investigating C_6H_5OH adsorption on catalytic Rh, $^{38, 42}$ Fe, 38 Pd, 38 and Pd-Fe facets. 95 Upon C₆H₅OH adsorption, there is significant elongation of the CAROMATIC-O bond of C6H5OH to 1.60 Å and 1.54 Å for Fe_1Mo_1P and $Fe_{1.5}Mo_{0.5}P$ compared to the $C_{AROMATIC}$ -O bond of gas-phase C₆H₅OH with optimized geometry (i.e., 1.43 Å). Notably, this elongation is more pronounced on Fe₁Mo₁P than on Fe_{1.5}Mo_{0.5}P due mainly to the greater Lewis acid character found on Fe₁Mo₁P (see section 3.2). The Fe₁Mo₁P can therefore turnover C₆H₅OH more rapidly than Fe_{1.5}Mo_{0.5}P because the C_{AROMATIC}-O in C₆H₅OH is weakened and C_{AROMATIC}-O bond cleavage is facilitated in the presence of H₂.

The $C_6H_5OH^*$ can then undergo transformation to benzene via the possible reaction mechanism discussed below. Of note, this section specifies adsorption and activation energies obtained during each elementary step via minimum energy pathways (MEPs), while primarily focusing on elementary steps only involving C_6H_5OH and its derivatives.

$$\begin{split} &C_{6}H_{5}OH(g)+\dot{\iota}_{..}C_{6}H_{5}OH^{\iota}(5)\\ &H_{2}(g)+2^{\iota}_{..}2H^{\iota}(6)\\ &C_{6}H_{5}OH^{\iota}+H^{\iota}_{..}C_{6}H_{5}^{\iota}+H_{2}O^{\iota}(7)\\ &C_{6}H_{5}^{\iota}+H^{\iota}C_{6}H_{5}^{\iota} rotationC_{6}H_{6}^{\iota}+\dot{\iota}^{\iota}\dot{\iota}_{.(8)}\\ &H_{2}O^{\iota}_{..}H_{2}O(g)+\dot{\iota}^{\iota}(9)\dot{\iota}\\ &C_{6}H_{6}^{\iota}_{..}C_{6}H_{6}(g)+\dot{\iota}^{\iota}(10)\dot{\iota} \end{split}$$

Following the generation of $C_6H_5OH^*$ and H^* species (Fig. 8 (a)-(b) and S6 (a)-(b); Eqn. (5)-(6)), the $C_6H_5OH^*$ is then subsequently dissociated to produce surface phenyl ($C_6H_5^*$) and hydroxyl species (OH*), during which the OH* is reacted with H* to generate H_2O adsorbed on surfaces (H_2O^* , Fig. 8 (c)-(d) and S6 (c)-(d); Eqn. (7)). The activation energy barriers required for this step are 0.39 eV for Fe_1Mo_1P and 0.77 eV for $Fe_{1.5}Mo_{0.5}P$. This demonstrates $C_{AROMATIC}$ -O bond scission is more favorable on Fe_1Mo_1P than $Fe_{1.5}Mo_{0.5}P$, which can result mainly from greater partial charge on metallic species for the Fe_1Mo_1P surface (*i.e.*, +0.81 |e|) compared to the $Fe_{1.5}Mo_{0.5}P$ surface (*i.e.*, +0.63 |e|). This again can be linked to enhanced surface Lewis acid

character on the Fe₁Mo₁P surface compared to the Fe_{1.5}Mo_{0.5}P surface. Subsequently, in the presence of H*, rotation of C₆H₅* takes place (Fig. 8 (e) and S6 (e)), exhibiting activation energy barriers of 0.11 eV and 0.21 eV for Fe₁Mo₁P and Fe_{1.5}Mo_{0.5}P, respectively. The activated C atom in C₆H₅* then faces towards the H*, which leads to the production of C₆H₅-H* species via C-H bond formation with the activation energy barriers of 0.26 eV for Fe_1Mo_1P and 0.51 eV for $Fe_{1.5}Mo_{0.5}P$ (Fig. 8 (f) and S6 (f); Eqn. (8)). This leads to the formation of $C_6H_6{}^{*}$ (Fig. 8 (g) and S6 (g) with adsorption energies of -1.68 eV for Fe₁Mo₁P and -2.18 eV for Fe_{1.5}Mo_{0.5}P) followed by desorption of C₆H₆ from the surfaces with desorption energy of 1.53 eV for Fe₁Mo₁P and 1.78 eV for Fe_{1.5}Mo_{0.5}P (Eqn. (10)). The formation of H₂O from H* and OH* species also requires activation energy barriers of 0.26 eV and 0.51 eV for Fe₁Mo₁P and Fe_{1.5}Mo_{0.5}P, respectively. It is evident that the C—O bond cleavage shows the greatest energy barriers among the three major elementary steps, thus assigning it as a rate-determining step in HDO1. In addition to HDO2 and HDO3 specified in the Supplementary Information, this mechanistic study demonstrates that Fe₁Mo₁P with a greater Lewis acid character can enhance TOFs compared to Fe-rich Fe_{1.5}Mo_{0.5}P. This is due mainly to lower activation energies for the ratedetermining steps for the transformation of phenol to benzene on Fe₁Mo₁P.

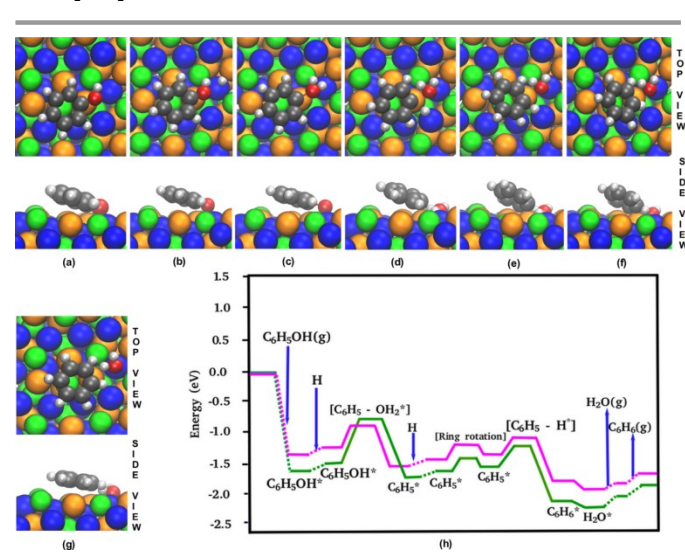


Fig. 8 Optimized structures of phenol (C_6H_5OH), benzene (C_6H_6), and reaction intermediates on the (112) facet for Fe_1Mo_1P during HDO1: (a) $C_6H_5OH^*$, (b) $C_6H_5OH^*$ and H^* , (c) $C_6H_5-OH_2^*$ (TS), (d) H^* , $C_6H_5^*$ and OH_2^* , (e) H^* , rotated $C_6H_5^*$, and H_2O^* , (f) $C_6H_5-H^*$ and H_2O^* , and (g) $C_6H_6^*$ and H_2O^* (orange for Fe; blue for Mo; green for P; grey for C; silver for H; red for O). (h) Reaction energetics on the (112) facet for Fe_1Mo_1P (magenta) and $Fe_{1.5}Mo_{0.5}P$ (green) during HDO1.

4. Conclusions

Herein, we have synthesized a series of iso-structural $Fe_xMo_{2\cdot x}P$ catalysts with $0.88 \le X \le 1.55$ and provided a detailed investigation of their surface properties via experimental and computational techniques. The bulk composition of the $Fe_xMo_{2\cdot x}P$ catalysts is capable of affecting the charge transfer phenomena among surface species, as evidenced by Bader

charge calculations on catalytic surface in these catalysts. The experimental and computational results suggested the highest charge transfer between the metals and phosphorus species occurs at X values of 0.99-1.14 and thus provides the greatest Lewis acid character, as evidenced by NH₃ TPD, CO-pulsed chemisorption experiments, and Bader charge analysis. From phenol HDO experiments, it was apparent that Fe_{0.99}Mo_{1.01}P and Fe_{1.14}Mo_{0.86}P could promote the TOFs for phenol consumption as well as provided higher benzene selectivity. DFT calculations provide evidence that these two catalysts can achieve desired coordination of the phenol on the catalytic surface, which is favorable to enhance the phenol HDO over the ring hydrogenation. These two catalysts, thus, improve the benzene selectivity in comparison with Fe-rich Fe_xMo_{2-x}P catalysts, which is also supported by time on stream study using benzonitrile as an in situ surface poisoner. DFT calculations provided further evidence for the mechanistic role of surface Lewis acid sites, which results in a lengthened C-O bond of adsorbed phenol on more Lewis acidic surfaces. This C-O bond elongation results in the subsequent C-O bond cleavage of phenol in the presence of H₂, reduces the activation energy, and ultimately promotes TOF values. This study provides more evidence that Lewis acid sites of the Fe_xMo_{2-x} catalysts can promote C-O bond cleavage reactions. Yet, surface Brønsted acid sites present on these catalysts may also participate in the reaction cycle, which is a topic of future study on these highly complex and fascinating bimetallic catalysts. The synthetic and analytic methodologies showcased in this study provide many benefits associated with the continued study of bimetallic phosphide catalysts for a variety of other metal combinations such as Co_xMo_{2-x}P, Ni_xMo₂₋ $_{x}P$, or $Ru_{x}Mo_{2-x}P$.

Acknowledgements

The experimental part of this work was funded through a NSF CAREER program (CBET# 1351609). Institutional support from Mississippi State University was used for the computational work. We thank Dr. Paul J. McGinn for use of his Jade software program. We acknowledge the Materials Characterization Facility and Center for Environmental Science & Technology at the University of Notre Dame for use of their XRD, XPS, and ICP-OES instruments. We also acknowledge VESTA, CANVAS, and VMD for use of their software to create images of the crystal structures contained in this report. All DFT calculations utilized computing resources at High Performance Computing Collaboratory at Mississippi State University. The DFT calculations also used resources of the National Energy Research Scientific Computing (NERSC) Center, a DOE Office of Science User Facility supported by the Office of Science of the U.S. Department of Energy under Contract No. of DE-AC02-05CH11231.

References

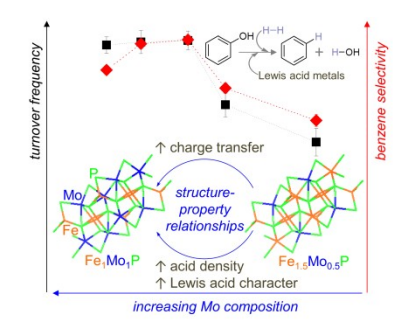
 Z. Fan, K. Sun and J. Wang, J. Mater. Chem. A, 2015, 3, 18809-18828.

- 2. M. Sharma, P. R. Pudasaini, F. Ruiz-Zepeda, E. Vinogradova and A. A. Ayon, *ACS Appl. Mater. Interfaces*, 2014, 6, 15472-15479.
- 3. S. B. Zhang, J. Phys.: Condens. Mat., 2002, 14, R881.
- 4. S. Zhou and H. Schmidt, *Materials*, 2010, 3, 5054.
- X. Peng, Q. Pan and G. L. Rempel, Chem. Soc. Rev., 2008, 37, 1619-1628.
- 6. R. Prins and M. E. Bussell, Catal. Lett., 2012, 142, 1413-1436.
- W. Yu, M. D. Porosoff and J. G. Chen, Chem. Rev., 2012, 112, 5780-5817.
- D. M. Alonso, S. G. Wettstein and J. A. Dumesic, Chem. Soc. Rev., 2012, 41, 8075-8098.
- 9. M. Sankar, N. Dimitratos, P. J. Miedziak, P. P. Wells, C. J. Kiely and G. J. Hutchings, *Chem. Soc. Rev.*, 2012, 41, 8099-8139.
- A.-M. Alexander and J. S. J. Hargreaves, Chem. Soc. Rev., 2010, 39, 4388-4401.
- 11. S. Carenco, D. Portehault, C. Boissière, N. Mézailles and C. Sanchez, *Chem. Rev.*, 2013, 113, 7981-8065.
- G. M. Arzac, T. C. Rojas and A. Fernández, *Appl. Catal. B*, 2012, 128. 39-47.
- T. G. Kelly and J. G. Chen, Chem. Soc. Rev., 2012, 41, 8021-8034
- 14. Y. N. Regmi and B. M. Leonard, *Chem. Mater.*, 2014, 26, 2609-2616.
- 15. J. M. Cameron, R. W. Hughes, Y. Zhao and D. H. Gregory, *Chem. Soc. Rev.*, 2011, 40, 4099-4118.
- 16. H. Wang, W. Li and M. Zhang, *Chem. Mater.*, 2005, 17, 3262-3267
- 17. F. Fu, Z. Cheng and J. Lu, RSC Adv., 2015, 5, 85395-85409.
- 18. A. Y. Bunch, X. Wang and U. S. Ozkan, *Appl. Catal. A*, 2008, 346, 96-103.
- 19. X. Wang, R. Y. Saleh and U. S. Ozkan, *J. Catal.*, 2005, 231, 20-
- 20. J. A. Rodriguez, Prog. Surf. Sci., 2006, 81, 141-189.
- 21. D. J. Rensel, S. Rouvimov, M. E. Gin and J. C. Hicks, *J. Catal.*, 2013, 305, 256-263.
- D. J. Rensel, J. Kim, Y. Bonita and J. C. Hicks, *Appl. Catal. A*, 2016, 524, 85-93.
- 23. S. Ted Oyama, H. Zhao, H.-J. Freund, K. Asakura, R. Włodarczyk and M. Sierka, *J. Catal.*, 2012, 285, 1-5.
- 24. A. Cho, J. Shin, A. Takagaki, R. Kikuchi and S. T. Oyama, *Top. Catal.*, 2012, 55, 969-980.
- A. F. Gaudette, A. W. Burns, J. R. Hayes, M. C. Smith, R. H. Bowker, T. Seda and M. E. Bussell, J. Catal., 2010, 272, 18-27.
- 26. A. W. Burns, A. F. Gaudette and M. E. Bussell, *J. Catal.*, 2008, 260, 262-269.
- 27. R. Wang and K. J. Smith, Catal. Lett., 2014, 144, 1594-1601.
- 28. K. Li, R. Wang and J. Chen, *Energy Fuels*, 2011, 25, 854-863.
- 29. I. Shirotani, M. Takaya, I. Kaneko, C. Sekine and T. Yagi, *Physica C*, 2001, 357–360, Part 1, 329-332.
- 30. I. I. Abu and K. J. Smith, *Catal. Today*, 2007, 125, 248-255.
- 31. Y.-K. Lee and S. T. Oyama, J. Catal., 2006, 239, 376-389.
- 32. A. P. Grosvenor, R. G. Cavell and A. Mar, *J. Solid State Chem.*, 2007, 180, 2702-2712.
- 33. P. E. R. Blanchard, A. P. Grosvenor, R. G. Cavell and A. Mar, *J. Mater. Chem.*, 2009, 19, 6015-6022.
- 34. E. Furimsky, Appl. Catal. A, 2000, 199, 147-190.
- 35. M. Badawi, J.-F. Paul, E. Payen, Y. Romero, F. Richard, S. Brunet, A. Popov, E. Kondratieva, J.-P. Gilson, L. Mariey, A.Travert and F. Maugé, *Oil Gas Sci. Technol.-Rev. IFP Energies nouvelles*, 2013, 68, 829-840.
- 36. E. O. Odebunmi and D. F. Ollis, J. Catal., 1983, 80, 56-64.
- 37. L. Nie, P. M. de Souza, F. B. Noronha, W. An, T. Sooknoi and D. E. Resasco, *J. Mol. Catal. A*, 2014, 388–389, 47-55.
- 38. A. J. R. Hensley, Y. Wang and J.-S. McEwen, *ACS Catal.*, 2015, 5, 523-536.

- 39. R. C. Nelson, B. Baek, P. Ruiz, B. Goundie, A. Brooks, M. C. Wheeler, B. G. Frederick, L. C. Grabow and R. N. Austin, *ACS Catal.*, 2015, 5, 6509-6523.
- 40. C.-c. Chiu, A. Genest, A. Borgna and N. Rosch, *Phys. Chem. Chem. Phys.*, 2015, 17, 15324-15330.
- 41. A. Robinson, G. A. Ferguson, J. R. Gallagher, S. Cheah, G. T. Beckham, J. A. Schaidle, J. E. Hensley and J. W. Medlin, *ACS Catal.*, 2016, 6, 4356-4368.
- 42. D. Garcia-Pintos, J. Voss, A. D. Jensen and F. Studt, *J. Phys. Chem. C*, 2016, 120, 18529-18537.
- 43. W. Yu, K. Xiong, N. Ji, M. D. Porosoff and J. G. Chen, *J. Catal.*, 2014, 317, 253-262.
- 44. J. Kim, A. G. Oliver, G. T. Neumann and J. C. Hicks, *Eur. J. Inorg. Chem.*, 2015, 2015, 3011-3018.
- 45. G. T. Neumann and J. C. Hicks, ACS Catal., 2012, 2, 642-646.
- 46. G. T. Neumann, B. R. Pimentel, D. J. Rensel and J. C. Hicks, *Catal. Sci. Technol.*, 2014, 4, 3953-3963.
- 47. J. Kim, M. S. Abbott, D. B. Go and J. C. Hicks, *ACS Energy Lett.*, 2016, 1, 94-99.
- R. G. Parr, in Horizons of Quantum Chemistry: Proceedings of the Third International Congress of Quantum Chemistry Held at Kyoto, Japan, October 29 - November 3, 1979, eds. K. Fukui and B. Pullman, Springer Netherlands, Dordrecht, 1980, DOI: 10.1007/978-94-009-9027-2 2, pp. 5-15.
- 49. A. D. Becke, J Chem. Phys., 2014, 140, 18A301.
- 50. G. Kresse and J. Hafner, Phys. Rev. B, 1993, 47, 558-561.
- 51. G. Kresse and J. Furthmüller, *Comput. Mater. Sci.*, 1996, 6, 15-50.
- 52. G. Kresse and J. Hafner, *Phys. Rev. B*, 1994, 49, 14251-14269.
- 53. G. Kresse and J. Furthmüller, *Phys. Rev. B*, 1996, 54, 11169-11186.
- 54. J. P. Perdew, J. A. Chevary, S. H. Vosko, K. A. Jackson, M. R. Pederson, D. J. Singh and C. Fiolhais, *Phys. Rev. B*, 1992, 46, 6671-6687.
- 55. J. P. Perdew and Y. Wang, *Phys. Rev. B*, 1992, 46, 12947-12954.
- J. P. Perdew, J. A. Chevary, S. H. Vosko, K. A. Jackson, M. R. Pederson, D. J. Singh and C. Fiolhais, *Phys. Rev. B*, 1993, 48, 4978-4978.
- P. E. Blöchl, O. Jepsen and O. K. Andersen, *Phys. Rev. B*, 1994, 49. 16223-16233.
- 58. G. Kresse and D. Joubert, *Phys. Rev. B*, 1999, 59, 1758-1775.
- 59. P. J. Stephens, F. J. Devlin, C. F. Chabalowski and M. J. Frisch, *J. Phys. Chem.*, 1994, 98, 11623-11627.
- M. Methfessel and A. T. Paxton, *Phys. Rev. B*, 1989, 40, 3616-3621.
- 61. D. J. Chadi and M. L. Cohen, Phys. Rev. B, 1973, 8, 5747-5753.
- G. Henkelman and H. Jónsson, J. Chem. Phys., 2000, 113, 9978-9985.
- G. Henkelman and H. Jónsson, J. Chem. Phys., 1999, 111, 7010-7022.
- 64. H. Jónsson, G. Mills and K. W. Jacobsen, in *Classical and Quantum Dynamics in Condensed Phase Simulations*, WORLD SCIENTIFIC, 2011, DOI: 10.1142/9789812839664_0016, pp. 385-404.
- 65. G. Henkelman, B. P. Uberuaga and H. Jónsson, *J. Chem. Phys.*, 2000, 113, 9901-9904.
- A. O. Oliynyk, Y. F. Lomnytska, M. V. Dzevenko, S. S. Stoyko and A. Mar, *Inorg. Chem.*, 2013, 52, 983-991.
- 67. T.-W. Shyr, J.-W. Shie, S.-J. Huang, S.-T. Yang and W.-S. Hwang, *Mater. Chem. Phys.*, 2010, 122, 273-277.
- K. Gebresellasie, J. C. Lewis and J. Shirokoff, *Energy Fuels*, 2013, 27, 2018-2024.
- A. R. Denton and N. W. Ashcroft, Phys. Rev. A, 1991, 43, 3161-3164.
- D. Ma, T. Xiao, S. Xie, W. Zhou, S. L. Gonzalez-Cortes and M. L. H. Green, *Chem. Mater.*, 2004, 16, 2697-2699.

- A. P. Grosvenor, S. D. Wik, R. G. Cavell and A. Mar, *Inorg. Chem.*, 2005, 44, 8988-8998.
- 72. V. M. L. Whiffen and K. J. Smith, *Energy Fuels*, 2010, 24, 4728-4737.
- 73. A. Y. Bunch and U. S. Ozkan, J. Catal., 2002, 206, 177-187.
- 74. D. C. Ghosh, T. Chakraborty and B. Mandal, *Theor. Chem.Acc.*, 2009, 124, 295-301.
- 75. A. L. Allred and E. G. Rochow, *J. Inorg. Nuc. Chem.*, 1958, 5, 264-268.
- A. P. Grosvenor, R. G. Cavell and A. Mar, J. Solid State Chem., 2008, 181, 2549-2558.
- 77. W. Tang, E. Sanville and G. Henkelman, *J. Phys.: Condens. Mat.*, 2009, 21, 084204.
- 78. E. Sanville, S. D. Kenny, R. Smith and G. Henkelman, *J. Comp. Chem.*, 2007, 28, 899-908.
- 79. G. Henkelman, A. Arnaldsson and H. Jónsson, *Comput. Mater. Sci.*, 2006, 36, 354-360.
- 80. M. Yu and D. R. Trinkle, J. Chem. Phys., 2011, 134, 064111.
- F. Hemmann, I. Agirrezabal-Telleria, C. Jaeger and E. Kemnitz, RSC Adv., 2015, 5, 89659-89668.
- 82. A. Vimont, J.-C. Lavalley, L. Francke, A. Demourgues, A. Tressaud and M. Daturi, *J. Phys. Chem. B*, 2004, 108, 3246-3255.
- 83. A. Seidel, A. Gutsze and B. Boddenberg, *Chem. Phys. Lett.*, 1997, 275, 113-118.
- V. A. Nasluzov, V. V. Rivanenkov, A. M. Shor, K. M. Neyman,
 U. Birkenheuer and N. Rösch, *Int. J. Quantum Chem.*, 2002, 90,
 386-402
- 85. A. M. Robinson, J. E. Hensley and J. W. Medlin, *ACS Catal.*, 2016, 6, 5026-5043.
- G. H. Gu, C. A. Mullen, A. A. Boateng and D. G. Vlachos, ACS Catal., 2016, 6, 3047-3055.
- 87. S. Zhu, Y. Qiu, Y. Zhu, S. Hao, H. Zheng and Y. Li, *Catal. Today*, 2013, 212, 120-126.
- 88. T. I. Korányi, Z. Vít, D. G. Poduval, R. Ryoo, H. S. Kim and E. J. M. Hensen, *J. Catal.*, 2008, 253, 119-131.
- 89. X. Song, Y. Ding, W. Chen, W. Dong, Y. Pei, J. Zang, L. Yan and Y. Lu, *Energy Fuels*, 2012, 26, 6559-6566.
- H. Lee, H. Kim, M. J. Yu, C. H. Ko, J.-K. Jeon, J. Jae, S. H. Park,
 S.-C. Jung and Y.-K. Park, Sci. Rep., 2016, 6, 28765.
- J. Jae, G. A. Tompsett, A. J. Foster, K. D. Hammond, S. M. Auerbach, R. F. Lobo and G. W. Huber, *J. Catal.*, 2011, 279, 257-268.
- 92. K. Zhang, L. Zhang, X. Chen, X. He, X. Wang, S. Dong, L. Gu, Z. Liu, C. Huang and G. Cui, ACS Appl. Mater. Interfaces, 2013, 5, 3677-3682.
- 93. W. Ji, R. Shen, R. Yang, G. Yu, X. Guo, L. Peng and W. Ding, *J. Mater. Chem. A*, 2014, 2, 699-704.
- 94. Y. Wang, D. Liu, Z. Liu, C. Xie, J. Huo and S. Wang, *Chem. Commun.*, 2016, 52, 12614-12617.
- J. Sun, A. M. Karim, H. Zhang, L. Kovarik, X. S. Li, A. J. Hensley,
 J.-S. McEwen and Y. Wang, J. Catal., 2013, 306, 47-57.

Graphical abstract



Compositional variation in $Fe_xMo_{2\,x}P$ catalysts alters their Lewis acidities, leading to modulated catalytic performance in the hydrodeoxygenation of phenol.